A Novel Data-Driven Physical Iterative Modeling Approach and Its Application in Quantum Instrumentation

Bodong Qin, Zhuo Wang, Wenfeng Fan, Ruigang Wang, Feng Li, and Wei Quan

***Abstract*—This work is the first to solve the data-driven modeling problem for quantum instrumentation and enables the model built is interpretable. First, a data-driven physical iteration (DPI) modeling approach is proposed to solve the modeling problem of a complex physical system with nonlinear characteristics based on the dynamic behavior of a quantum system described by the phenomenological rate equation. Second, the proposed DPI modeling approach incorporates the fast sampling technique, which is proved feasible by the Taylor mean value theorem, to solve the modeling problem of a nonautonomous system. Third, the convergence of the proposed approach is proved by the least squares criterion and the law of large numbers. Finally, the DPI modeling approach is deployed in the optically pumped magnetometer (OPM) and spin-exchange relaxation-free comagnetometer (SERFCM), the physical parameters of the system are estimated while the quantum instrumentation modeling is completed. Numerical simulations and practical experiments support the theoretical results.**

***Index Terms*—Data-driven, optically pumped magnetometer (OPM), parameter identification, quantum instrumentation, spin-exchange relaxation-free comagnetometer (SERFCM).**

I. Introduction

QUANTUM instrumentations [1] are frontier physical measurement devices founded on information technology and quantum physics, for example, atomic clock [2], optically pumped magnetometer (OPM) [3], and spin-exchange relaxation-free comagnetometer (SERFCM) [4], [5]. The development of quantum instrumentations with high precision [6] and small size [7] is important for medical imaging [8], inertial rotation sensing [9], and magnetometry [10]. In particular, accurate system modeling is a crucial problem in quantum instrumentations to enhance the measurement precision, facilitate error suppression [11] and feedback control [12], [13]. Scholars typically model quantum systems based on the atomic spin effect in terms of physical mechanisms or engineering applications. For instance, the density matrix modeling approach is based on quantum mechanics [14], the Bloch equation modeling approach is based on simplifying the density matrix [15], and the transfer function modeling approach is based on system identification [16]. These approaches can be particularly effective in specific situations, but they also have weaknesses. For example, the density matrix is based on the Hamiltonian formulation, which is complex and difficult to calculate and solve. The Bloch equation does not represent the full system dynamics and is not well adapted to practice because of the lack of factors, such as temperature term in the equation. The transfer function is only valid at the equilibrium point and cannot be worked for complex nonlinear systems. Hence, we need to discover a modeling approach that is convenient to use and effectively exploits the properties of complex physical systems to overcome these difficulties.

Data-driven modeling has been a neoteric system modeling approach in recent decades [17]. Compared with the traditional scientific mechanical modeling approach, this approach can complete the modeling work without any prior knowledge, such as the neural networks [18], *k*-nearest neighbors [19], and support vector machines [20]. However, applying a data-driven approach to accurately model complex physical systems often requires data from multiple processes [21], and the

Manuscript received 5 December 2023; revised 28 February 2024; accepted 28 May 2024. Date of publication 24 June 2024; date of current version 20 August 2024. This work was supported in part by the National Natural Science of China (NSFC) for Distinguished Young Scholars under Grant 61925301; in part by the Innovation Program for Quantum Science and Technology under Grant 2021ZD0300402; in part by the National Natural Science Foundation of China (NSFC) under Grant 62103026 and Grant 61673041; and in part by the Key Area Research and Development Program of Guangdong Province under Grant 2021B0101410005. This article was recommended by Associate Editor R. Wisniewski. *(Corresponding author: Ruigang Wang.)*

Bodong Qin is with the School of Information Science and Technology, Hangzhou Normal University, Hangzhou 311121, China, and also with the School of Instrumentation and Optoelectronic Engineering, Beihang University, Beijing 100191, China.

Zhuo Wang is with the School of Instrumentation and Optoelectronic Engineering, Institute of Large-scale Scientific Facility, and Centre for Zero Magnetic Field Science, Beihang University, Beijing 100191, China.

Wenfeng Fan, Feng Li, and Wei Quan are with the School of Instrumentation and Optoelectronics Engineering, Institute of Large-scale Scientific Facility, and Centre for Zero Magnetic Field Science, Beihang University, Beijing 100191, China, also with Hefei National Laboratory, Hefei 230088, China, and also with the National Institute of Extremely-Weak Magnetic Field Infrastructure, Hangzhou 310051, China.

Ruigang Wang is with the School of Information Science and Technology, Hangzhou Normal University, Hangzhou 311121, China (e-mail: ruigangwang@buaa.edu.cn).

Color versions of one or more figures in this article are available at https://doi.org/10.1109/TSMC.2024.3408872.

Digital Object Identifier 10.1109/TSMC.2024.3408872

dataset for each process is commonly relatively large [22]. This situation undoubtedly increases the complexity of the practical application, especially for quantum instrumentations requiring miniaturization. When confronted with this type of problem, some scholars suggested solutions based on selecting the appropriate dataset [23], determining the optimal modeling parameters [24], and choosing the proper modeling approach [25]. Although the above approaches are practical, the models still suffer interpretability [26], especially in describing the dynamic evolution of complex physical systems [27]. Therefore, combining the ability of data-driven exploit system characteristics with the interpretability of physical laws for system modeling has become the key to solving such problems. In this article, we present a data-driven physical iterative (DPI) modeling approach for solving complex physical system modeling problems using finite datasets, which can be combined with physical laws to uncover the intrinsic mechanisms of the system. This approach allows theoretically bridging the gap between theoretical and practical models to analyze the evolutionary processes of complex physical systems comprehensively.

The significant contributions of this article are listed as follows. First, this article is the first to solve the data-driven modeling problem in quantum instrumentation, which fills the gap in data-driven modeling approaches. Second, based on the fast sampling technique, a DPI modeling approach is proposed to solve the modeling problem of a nonlinear system. This approach combines prior physical knowledge and engineering experience to ensure that the model is interpretable. Third, the convergence of the approach under different noise interference conditions is proved based on the least squares criterion and the law of large numbers. Finally, simulations and experiments verify that the approach is effective in quantum instrumentation. The effectiveness of the proposed approach lies in the following aspects: 1) the excitation signal is self-designed, which breaks the limitations of the traditional quantum instrumentation modeling approach [16]; 2) this approach, which is suitable for nonlinear nonautonomous systems, exhibits higher accuracy and smaller error in the experiment when compared with the approach in [28]; and 3) in the proposed approach, all unknown system parameters can be online estimated simultaneously, which is superior to the parameter measurement of traditional physical experiments [29], [30], [31].

The remainder of the work is organized as follows. The model foundations, including physical and control models of quantum system, are given in Section II. The algorithmic framework and implementation of the DPI modeling approaches are developed in Section III. The convergence analysis of the proposed approach is given in Section IV. The simulation and the experiment are presented in Sections V and VI, respectively. Finally, Section VII concludes this article.

This article utilizes the standard mathematical notations. Let $\mathbb{R}$ denote the set of real numbers, $\overline{\mathbb{R}}_+$ denote the set of nonnegative numbers, $\boldsymbol{A}^{-1}$ represents the inverse of the matrix $\boldsymbol{A}$, $\boldsymbol{A}^{\mathrm{T}}$ represent the transpose of the matrix $\boldsymbol{A}$, $\|\cdot\|_2$ denote the Frobenius norm, $\lceil\cdot\rceil$ denotes upward rounding.

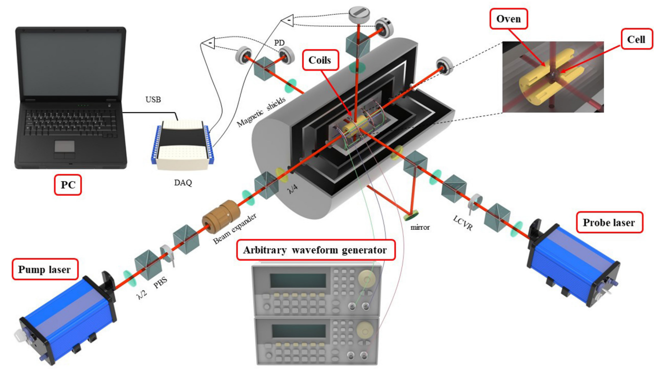

Fig. 1. Structure of the quantum system. LCVR: liquid crystal variable retarder, PBS: polarizing beam splitter, DAQ: data acquisition system, and PC: personal computer.

II. Problem Description and Preliminaries

In this section, the physical model of quantum system based on atomic spin effects is described and turned into a nonlinear nonautonomous system with multiple inputs and outputs.

A. Quantum System Description

The quantum system generally comprises a spherical glass gas cell containing single or multiple species of atoms, magnetic coils, an oven, and lasers. The system polarizes specific atoms with a pump beam and measures their spin polarization by probing beams. The physical equipment used to generate the experimental data is shown schematically in Fig. 1.

In the spherical glass gas cell, we typically monitor the spins of $10^{12} - 10^{14}$ or more atoms, each of which can be depicted by a wavefunction. However, if we wish to model the time evolution of the ensemble of atomic spins, it is impossible to model the evolution of so many independent wavefunctions. Instead, we require another approach of determining the statistical average of the spin operator. Therefore, we describe the state of the ensemble of spins using the phenomenological rate equation, which can be written in a general form as

$$\frac{\mathrm{d}}{\mathrm{d}t}\boldsymbol{S} = \frac{i}{\hbar}[\boldsymbol{\mathcal{H}}, \boldsymbol{S}] - R_{\mathrm{tot}} \cdot (\boldsymbol{S} - \boldsymbol{S}_0). \tag{1}$$

Here, $\boldsymbol{S} = [S_x, S_y, S_z]^{\mathrm{T}}$ represents the spin polarization of the atoms in the coordinate system (x, y, z), ranging from 0 to 1 in each direction. The term R_{tot} denotes the relaxation rate of the atoms, and $\boldsymbol{S}_0 = [S_{x0}, S_{y0}, S_{z0}]^{\mathrm{T}}$ signifies the steady-state polarization, reflecting the interaction between light and atoms. The symbol $[\cdot, \cdot]$ designates the commutator operation. The Hamiltonian $\boldsymbol{\mathcal{H}}$ describes the coupling of the electron spin to a magnetic field and is expressed in the rotating frame as

$$\boldsymbol{\mathcal{H}} = \gamma\hbar\boldsymbol{B} \cdot \boldsymbol{S} + \hbar\boldsymbol{\Omega} \cdot \boldsymbol{S}. \tag{2}$$

Here, γ is the gyromagnetic ratio. $\hbar$ is the reduced Planck constant. $\boldsymbol{B} = [B_x, B_y, B_z]^{\mathrm{T}}$ and $\boldsymbol{\Omega} = [\Omega_x, \Omega_y, \Omega_z]^{\mathrm{T}}$ are the magnetic field and angular rate felt by the atoms, respectively.

Equations (1) and (2) only represent the dynamic behavior of single species atoms. However, quantum instrumentations frequently contain different species of atoms, i.e., the dimensionality of the differential (1) increases exponentially. At this point, the interactions between atoms become exceptionally complex, and the system exhibits solid nonlinear characteristics. Moreover, the atomic spin dynamics equations described using the laws of physics are universal and cannot be better applied to practical working situations. This makes it challenging to accurately describe the practical systems with physical models.

B. Control System Description

In response to the problem discussed in the preceding section, this section describes practical quantum systems as unknown nonlinear nonautonomous systems with multiple inputs and outputs, aiming to fully explore the intrinsic mechanisms of quantum systems, as follows:

$$\dot{\boldsymbol{x}}(t) = f(\boldsymbol{x}, \boldsymbol{u}, t) \quad t \in \bar{\mathbb{R}}_+ \tag{3}$$

where $f(\boldsymbol{x}, \boldsymbol{u}, t) : \mathbb{R}^n \times \mathbb{R}^m \times \mathbb{R} \to \mathbb{R}^n$ is a smooth mapping following the standard notation; the state $\boldsymbol{x}(t) \in \mathbb{R}^n$ and input $\boldsymbol{u}(t) \in \mathbb{R}^m$ of above system defined as follows:

$$\boldsymbol{x}(t) = \begin{bmatrix} x_1(t) \\ x_2(t) \\ \vdots \\ x_n(t) \end{bmatrix}, \quad \boldsymbol{u}(t) = \begin{bmatrix} u_1(t) \\ u_2(t) \\ \vdots \\ u_m(t) \end{bmatrix}. \tag{4}$$

Consider a fixed time interval $[0, T_f]$ and an equally spaced partition $0 \equiv t_0 < t_1 < t_2 < \cdots < t_N \equiv T_f$. Based on the Euler method, we can obtain the discrete model of the nonlinear system as follow:

$$\boldsymbol{x}(t_{k+1}) = \boldsymbol{x}(t_k) + f(\boldsymbol{x}(t_k), \boldsymbol{u}(t_k), t_k)\Delta T \tag{5}$$

where $\Delta T = t_{k+1} - t_k,\ k = 0, 1, \ldots, N-1$ is the discrete time.

III. Data-Driven Physical Iterative Modeling Approach

Considering the theoretical model (1) and the practical model (3) of the quantum instrumentation, we can design a high-precision detection module, which utilizes the birefringence and light absorption effects to capture the atomic spin polarization state $\boldsymbol{x}(t)$, and at the same time, uses the photoelectric converter and data acquisition system to obtain the system input $\boldsymbol{u}(t)$. Furthermore, we can define the input library matrix as follows:

$$\mathcal{C}(t) = \left[1, \boldsymbol{u}^{\mathrm{T}}(t), c\left(\boldsymbol{u}^{\mathrm{T}}(t)\right)\right] \tag{6}$$

where the elements in the matrix $c(\boldsymbol{u}^{\mathrm{T}}(t))$ cover all possible nonlinear input forms in the system, such as $c(\boldsymbol{u}^{\mathrm{T}}(t)) = [\sin(u_1(t)), (u_2(t))^3, \ldots]$. Similarly, the state library matrix is defined as

$$\mathcal{G}(t) = \left[\boldsymbol{x}^{\mathrm{T}}(t), g\left(\boldsymbol{x}^{\mathrm{T}}(t)\right)\right] \tag{7}$$

where the elements in the matrix $g(\boldsymbol{x}^{\mathrm{T}}(t))$ cover all possible nonlinear state forms in the system.

Based on (6) and (7), we can always construct the discrete model (5) for nonlinear nonautonomous systems as follows:

$$\boldsymbol{x}(t_{k+1}) = \boldsymbol{\theta}(t_k)\boldsymbol{e}(\boldsymbol{x}(t_k), \boldsymbol{u}(t_k), \boldsymbol{I}_{1\times1}) \tag{8}$$

where $\boldsymbol{\theta}(t_k) \in \mathbb{R}^{n\times j}$ $(j \geq n(m+1) - 1)$ is defined as the parameter matrix of the system; and $\boldsymbol{e}(\boldsymbol{x}(t_k), \boldsymbol{u}(t_k), \boldsymbol{I}_{1\times1}) \in \mathbb{R}^j$ is defined as the nonlinear combinatorial matrix of the system as follows:

$$\boldsymbol{e}(\boldsymbol{x}(t_k), \boldsymbol{u}(t_k), \boldsymbol{I}_{\mathbf{1}\times\mathbf{1}}) = \left[\mathcal{C}(t_k) \otimes \mathcal{G}(t_k), \boldsymbol{I}_{1\times1}\right]^{\mathrm{T}} \tag{9}$$

where $\boldsymbol{I}_{1\times1}$ represents the identity matrix and $\otimes$ denotes the tensor product.

A. Autonomous System

Before delving into nonautonomous system modeling, we start by modeling and analyzing autonomous systems. In this circumstances, the parameter matrix $\boldsymbol{\theta}(t_k)$ is independent of time, i.e., $\boldsymbol{\theta}(t_k) = \boldsymbol{\theta}$, then (8) can be written as

$$\boldsymbol{x}(t_{k+1})^{\mathrm{T}} = \boldsymbol{e}(\boldsymbol{x}(t_k), \boldsymbol{u}(t_k), \boldsymbol{I}_{1\times1})^{\mathrm{T}}\boldsymbol{\theta}^{\mathrm{T}}. \tag{10}$$

Given the initial value $\boldsymbol{u}(t_0)$ and $\boldsymbol{x}(t_0)$, iterate p times based on the above equation and the following matrix equation can be constructed

$$\begin{bmatrix} \boldsymbol{x}\left(t_p\right)^{\mathrm{T}} \\ \boldsymbol{x}\left(t_{p-1}\right)^{\mathrm{T}} \\ \vdots \\ \boldsymbol{x}(t_1)^{\mathrm{T}} \end{bmatrix} = \begin{bmatrix} \boldsymbol{e}\left(\boldsymbol{x}\left(t_{p-1}\right), \boldsymbol{u}\left(t_{p-1}\right), \boldsymbol{I}_{1\times1}\right)^{\mathrm{T}} \\ \boldsymbol{e}\left(\boldsymbol{x}\left(t_{p-2}\right), \boldsymbol{u}\left(t_{p-2}\right), \boldsymbol{I}_{1\times1}\right)^{\mathrm{T}} \\ \vdots \\ \boldsymbol{e}(\boldsymbol{x}(t_0), \boldsymbol{u}(t_0), \boldsymbol{I}_{1\times1})^{\mathrm{T}} \end{bmatrix} \boldsymbol{\theta}^{\mathrm{T}} \tag{11}$$

where the left side of the equation represents the system state iteration matrix and the first matrix on the right represents the system nonlinear combinatorial iteration matrix. For convenience, (11) is written as

$$\boldsymbol{X_p} = \boldsymbol{E_p}\boldsymbol{\theta}^{\mathrm{T}}. \tag{12}$$

Thus, the challenge of modeling and identifying an unknown nonlinear system translates into solving the matrix $\boldsymbol{\theta}^{\mathrm{T}}$. Next, we will analyze this in three cases.

Case 1: Rank($\boldsymbol{E_p}$) = Rank($\boldsymbol{E_p}, \boldsymbol{X_p}$) = $p < j$:

Definition 1 (Generalized Inverse of a Matrix): There is a matrix $\boldsymbol{E_p^-} \in \mathbb{R}^{j\times p}$ defined as a generalized inverse matrix of $\boldsymbol{E_p}$, which satisfies $\boldsymbol{\theta}^{\mathrm{T}} = \boldsymbol{E_p^-}\boldsymbol{X_p}$. If the matrix (12) has solutions, i.e., $\mathrm{Rank}(\boldsymbol{E_p}) = \mathrm{Rank}(\boldsymbol{E_p}, \boldsymbol{X_p})$ holds.

Based on Definition 1 and [32], the estimates of the parameter matrix is analyzed in the following lemma.

Lemma 1: Let $\boldsymbol{E_p^-}$ be the generalized inverse matrix of $\boldsymbol{E_p}$, then the general form of the estimated value of the parameter matrix in matrix (12) can be expressed as

$$\widehat{\boldsymbol{\theta}^{\mathrm{T}}} = \boldsymbol{E_p^-}\boldsymbol{X_p} + \left(\boldsymbol{I}_{j\times j} - \boldsymbol{E_p^-}\boldsymbol{E_p}\right)\boldsymbol{Z} \tag{13}$$

where $\boldsymbol{Z} \in \mathbb{R}^{j\times n}$ is an arbitrary matrix.

Proof: Multiply both sides of (13) by $\boldsymbol{E_p}$ on the left, we have

$$\begin{aligned} \boldsymbol{E_p}\widehat{\boldsymbol{\theta}^{\mathrm{T}}} &= \boldsymbol{E_p}\boldsymbol{E_p^-}\boldsymbol{X_p} + \boldsymbol{E_p}\left(\boldsymbol{I}_{j\times j} - \boldsymbol{E_p^-}\boldsymbol{E_p}\right)\boldsymbol{Z} \\ &= \boldsymbol{E_p}\boldsymbol{E_p^-}\boldsymbol{X_p}. \end{aligned} \tag{14}$$

From Definition 1, there exists the equation $\widehat{\boldsymbol{\theta}}^{\mathrm{T}} = \boldsymbol{E}_p^{-}\boldsymbol{X}_p$, and hence (13) is the general solution of (12).

Also, if $\widetilde{\boldsymbol{\theta}}^{\mathrm{T}}$ is an arbitrary solution of (12), let $\boldsymbol{Z} = \widetilde{\boldsymbol{\theta}}^{\mathrm{T}} - \boldsymbol{E}_p^{-}\boldsymbol{X}_p$ and we get

$$\begin{aligned}\left(\boldsymbol{I}_{j\times j} - \boldsymbol{E}_p^{-}\boldsymbol{E}_p\right)\boldsymbol{Z} &= \left(\boldsymbol{I}_{j\times j} - \boldsymbol{E}_p^{-}\boldsymbol{E}_p\right)\left(\widetilde{\boldsymbol{\theta}}^{\mathrm{T}} - \boldsymbol{E}_p^{-}\boldsymbol{X}_p\right)\\ &= \widetilde{\boldsymbol{\theta}}^{\mathrm{T}} - \boldsymbol{E}_p^{-}\boldsymbol{X}_p - \boldsymbol{E}_p^{-}\boldsymbol{X}_p + \boldsymbol{E}_p^{-}\boldsymbol{X}_p \end{aligned} \tag{15}$$

then (13) holds. This completes the proof of Lemma 1. ■

Case 2: Rank($\boldsymbol{E_p}$) = Rank($\boldsymbol{E_p}, \boldsymbol{X_p}$) = $p = j$:

In this case, $\boldsymbol{E_p}$ is a full rank square matrix, i.e., there exists a unique invertible matrix $\boldsymbol{E}_p^{-1}$ of $\boldsymbol{E_p}$. Therefore, the system parameter matrix can be directly estimated as

$$\widehat{\boldsymbol{\theta}}^{\mathrm{T}} = \boldsymbol{E}_p^{-1}\boldsymbol{X}_p. \tag{16}$$

Case 3: Rank($\boldsymbol{E_p}$) = $j <$ Rank($\boldsymbol{E_p}, \boldsymbol{X_p}$) $\le p$:

Definition 2 (The Least Squares Solution): We define $\boldsymbol{\theta}_{ls}^{\mathrm{T}}$ as the least squares solution in (12), if we can make it satisfy $\|\boldsymbol{X_p} - \boldsymbol{E_p}\boldsymbol{\theta}_{ls}^{\mathrm{T}}\|_2{}^2 = \min \|\boldsymbol{X_p} - \boldsymbol{E_p}\boldsymbol{\theta}^{\mathrm{T}}\|_2{}^2$. When the matrix (12) has no solution, i.e., $\mathrm{Rank}(\boldsymbol{E_p}) \neq \mathrm{Rank}(\boldsymbol{E_p}, \boldsymbol{X_p})$.

By Definition 2 and [32], the estimates of the parameter matrix is analyzed in the following lemma.

Lemma 2: There exists a unique least squares solution $\widehat{\boldsymbol{\theta}}^{\mathrm{T}} = \left(\boldsymbol{E}_p^{\mathrm{T}}\boldsymbol{E}_p\right)^{-1}\boldsymbol{E}_p^{\mathrm{T}}\boldsymbol{X}_p$ as the estimate of the parameter matrix in (12) if it satisfies $\mathrm{Rank}(\boldsymbol{E_p}) \neq \mathrm{Rank}(\boldsymbol{E_p}, \boldsymbol{X_p})$.

Proof: First, we define the cost function as

$$\begin{aligned}\boldsymbol{J} &= \left\|\boldsymbol{X}_p - \boldsymbol{E}_p\widehat{\boldsymbol{\theta}}^{\mathrm{T}}\right\|_2^2\\ &= \boldsymbol{X}_p^{\mathrm{T}}\boldsymbol{X}_p - \widehat{\boldsymbol{\theta}}^{\mathrm{T}}\boldsymbol{E}_p^{\mathrm{T}}\boldsymbol{X}_p - \boldsymbol{X}_p^{\mathrm{T}}\boldsymbol{E}_p\widehat{\boldsymbol{\theta}}^{\mathrm{T}} + \widehat{\boldsymbol{\theta}}^{\mathrm{T}}\boldsymbol{E}_p^{\mathrm{T}}\boldsymbol{E}_p\widehat{\boldsymbol{\theta}}^{\mathrm{T}}. \end{aligned} \tag{17}$$

This cost function is a concave function with $\widehat{\boldsymbol{\theta}}^{\mathrm{T}}$ variable over the entire interval of real numbers and it is minimized only when $\widehat{\boldsymbol{\theta}}^{\mathrm{T}}$ approaches the least squares solution point. Thus, the optimization process can be designed as follows:

$$\frac{\partial \boldsymbol{J}}{\partial \widehat{\boldsymbol{\theta}}^{\mathrm{T}}} = -2\boldsymbol{E}_p^{\mathrm{T}}\boldsymbol{X}_p + 2\boldsymbol{E}_p^{\mathrm{T}}\boldsymbol{E}_p\widehat{\boldsymbol{\theta}}^{\mathrm{T}}. \tag{18}$$

Next, the least squares solution to (12) is obtained when the above equation is zero as

$$\boldsymbol{E}_p^{\mathrm{T}}\boldsymbol{E}_p\widehat{\boldsymbol{\theta}}^{\mathrm{T}} = \boldsymbol{E}_p^{\mathrm{T}}\boldsymbol{X}_p. \tag{19}$$

Finally, it follows from (9) that $\boldsymbol{E_p}$ is a column full rank matrix, i.e., $\left(\boldsymbol{E}_p^{\mathrm{T}}\boldsymbol{E}_p\right)^{-1}$ exists. At this point, the least squares solution of (12) has a unique value and is defined as an estimate of the system parameters, as follows:

$$\widehat{\boldsymbol{\theta}}^{\mathrm{T}} = \left(\boldsymbol{E}_p^{\mathrm{T}}\boldsymbol{E}_p\right)^{-1}\boldsymbol{E}_p^{\mathrm{T}}\boldsymbol{X}_p. \tag{20}$$

This completes the proof of Lemma 2. ■

In the end, the discrete expression of the quantum system after modeling and identification is as follows:

$$\boldsymbol{x}(t_{k+1}) = \widehat{\boldsymbol{\theta}}\boldsymbol{e}(\boldsymbol{x}(t_k), \boldsymbol{u}(t_k), \boldsymbol{I}_{1\times 1}). \tag{21}$$

In numerical computation, the singular value decomposition [33] is typically used to compute the generalized inverse of a matrix. Therefore, the time complexity of the whole algorithm can be expressed as $O(\min(p^2 j, pj^2) + pjn)$, and its main steps are summarized in Algorithm 1.

Algorithm 1 DPI Algorithm for Autonomous System

Input: The set of sampled data $\{\boldsymbol{x}(p), \boldsymbol{u}(p)\}$.
Output: The estimate of the parameter $\widehat{\boldsymbol{\theta}}^{\mathrm{T}}$;
1: Specifies the initial number of iterations $p = 1$.
2: **while** $p \le N$(N is the size of the sample data) **do**
3: Collect sampled data $\{\boldsymbol{x}(p), \boldsymbol{u}(p)\}$;
4: Establish nonlinear combinatorial data sets $\boldsymbol{e}(\boldsymbol{x}(t_p), \boldsymbol{u}(t_p), \boldsymbol{I}_{1\times 1})$ in (9);
5: Establish iterative data matrix $\boldsymbol{X_p}$ and $\boldsymbol{E_p}$ in (11) and (12);
6: **if** $p < j$ **then**
7: Calculate and update the estimated system parameter matrix $\widehat{\boldsymbol{\theta}}^{\mathrm{T}}$ in (13);
8: **else if** $p = j$
9: Calculate and update the estimated system parameter matrix $\widehat{\boldsymbol{\theta}}^{\mathrm{T}}$ in (16);
10: **else**
11: Calculate and update the estimated system parameter matrix $\widehat{\boldsymbol{\theta}}^{\mathrm{T}}$ in (20);
12: **end if**
13: Increase p by 1;
14: **end while**
15: **return** $\widehat{\boldsymbol{\theta}}^{\mathrm{T}}$;

B. Nonautonomous System

In practical working conditions, the quantum instrumentation is typically a nonautonomous system with its parameter matrix $\boldsymbol{\theta}(t_k)$ being a function of time. Consequently, (8) can be expressed as

$$\boldsymbol{x}(t_{k+1})^{\mathrm{T}} = \boldsymbol{e}(\boldsymbol{x}(t_k), \boldsymbol{u}(t_k), \boldsymbol{I}_{1\times 1})^{\mathrm{T}}\boldsymbol{\theta}(t_k)^{\mathrm{T}}. \tag{22}$$

Based on the application of the DPI algorithm in autonomous system, a fast sampling technique is given to solve the problem of online updating of system parameters. First, the following theorem is presented.

Theorem 1: For a system parameter matrix $\boldsymbol{\theta}^{\mathrm{T}}(t)$ in (8) that varies slowly with time t, if $\|\partial\boldsymbol{\theta}(t)^{\mathrm{T}}/\partial t\|_2 < \kappa$ holds, where the constant κ represents the parameter rate of variation boundary. Then there exists a time interval $T > 0$ such that within $[t_m, t_m + T]$, for any given $\varepsilon > 0$, we have $\|\boldsymbol{\theta}^{\mathrm{T}}(t) - \boldsymbol{\theta}^{\mathrm{T}}(t_m)\|_2 < \varepsilon$.

Proof: Following Taylor mean value theorem, the parameter matrix $\boldsymbol{\theta}^{\mathrm{T}}(t)$ has higher-order derivatives in the time interval $[t_m, t_m + T]$, then for any $t_m \ge 0$, there is a first order Taylor expansion as

$$\boldsymbol{\theta}^{\mathrm{T}}(t) = \boldsymbol{\theta}^{\mathrm{T}}(t_m) + \frac{\partial\boldsymbol{\theta}^{\mathrm{T}}(t)}{\partial t}(t - t_m) + \boldsymbol{o}(t - t_m) \tag{23}$$

where $\boldsymbol{o}(t - t_m)$ is a higher-order infinitesimal, and so

$$\|\boldsymbol{\theta}^{\mathrm{T}}(t) - \boldsymbol{\theta}^{\mathrm{T}}(t_m)\|_2 = \|\frac{\partial\boldsymbol{\theta}^{\mathrm{T}}(t)}{\partial t}(t - t_m) + \boldsymbol{o}(t - t_m)\|_2$$

$$
\begin{aligned}
&< \left\|\frac{\partial \boldsymbol{\theta}^{\mathrm{T}}(t)}{\partial t}\right\|_2 (t-t_m) + \|\boldsymbol{o}(t-t_m)\|_2 \\
&< \kappa T + \|\boldsymbol{o}(T)\|_2. \qquad (24)
\end{aligned}
$$

Thus, for any given $\varepsilon > 0$, there always exists a time interval T that satisfies $\|\boldsymbol{\theta}^{\mathrm{T}}(t) - \boldsymbol{\theta}^{\mathrm{T}}(t_m)\|_2 < \varepsilon$.

This completes the proof of Theorem 1. ■

Corollary 1: Let $\widehat{\boldsymbol{\theta}}^{\mathrm{T}}(t_k)$ represent the parameter estimate obtained by applying Algorithm 1 to system (22) within the time interval $[t_{k+1} - T, t_{k+1}]$, where $(t_{k+1} \geq T)$. Then, the error in system parameter estimation can be expressed as $e = \|\boldsymbol{\theta}^{\mathrm{T}}(t) - \widehat{\boldsymbol{\theta}}^{\mathrm{T}}(t_k)\|_2 < \varepsilon$.

Proof: Based on Lemma 2 and Theorem 1, we can obtain the cost function in the time interval $[t_{k+1} - T, t_{k+1}]$ as follows:

$$
\begin{aligned}
J = \left\|\boldsymbol{X_p} - \boldsymbol{E_p}\widehat{\boldsymbol{\theta}}^{\mathrm{T}}(t_k)\right\|_2 &= \min\left\|\boldsymbol{X_p} - \boldsymbol{E_p}\boldsymbol{\theta}^{\mathrm{T}}\right\|_2 \\
&< \left\|\boldsymbol{X_p} - \boldsymbol{E_p}\boldsymbol{\theta}^{\mathrm{T}}(t_{k+1} - T)\right\|_2 < \left\|\boldsymbol{E_p}\varepsilon\right\|_2. \qquad (25)
\end{aligned}
$$

Therefore, we can derive the following error function:

$$
e = \|\boldsymbol{\theta}^{\mathrm{T}}(t) - \widehat{\boldsymbol{\theta}}^{\mathrm{T}}(t_k)\|_2 \leq \|\boldsymbol{\theta}^{\mathrm{T}}(t) - \boldsymbol{\theta}^{\mathrm{T}}(t_{k+1} - T)\|_2 < \varepsilon. \quad (26)
$$

The proof is completed. ■

Finally, the discrete form of the quantum system, after nonautonomous modeling and identification, is as follows:

$$
\boldsymbol{x}(t_{k+1}) = \widehat{\boldsymbol{\theta}}(t_k)\boldsymbol{e}(\boldsymbol{x}(t_k), \boldsymbol{u}(t_k), \boldsymbol{I}_{1\times 1}). \qquad (27)
$$

With the proliferation of high-speed analog-to-digital converters (ADCs), high-speed processors, and memory technologies, we can sample input and output signals from the system at higher frequencies and store these measurements, thereby facilitating accurate estimation of the system parameter matrix over a time interval T. The new sampling period is denoted as τ ($\tau = [\Delta T/s]$, where s is a positive integer). Consequently, the time complexity remains bounded by $O(N(\min((T/\tau)^2 j, (T/\tau)j^2) + (T/\tau)jn))$, where N represents the number of parameter estimation. It is important to note that the time interval between two consecutive estimations of the parameter matrix $\boldsymbol{\theta}(t_k)$ remains ΔT. The detailed steps are elaborated in Algorithm 2.

Algorithm 2 DPI Algorithm for Nonautonomous System

Input: The set of sampled data $\{\boldsymbol{x}(k), \boldsymbol{u}(k)\}$.
Output: The estimate of the parameter $\widehat{\boldsymbol{\theta}}^{\mathrm{T}}(k)$;
1: Specify initial sampling number $k = 1$;
2: Establish nonlinear combinatorial data sets $\boldsymbol{e}(\boldsymbol{x}(k), \boldsymbol{u}(k), \boldsymbol{I}_{1\times 1})$ in (9);
3: **while** $k \leq T/\Delta T$ **do**
4: Specifies the initial number of iterations $p = 1$ and data length $N_T = k \cdot \Delta T/\tau$;
5: Collecting the sampled data $\{\boldsymbol{x}(p), \boldsymbol{u}(p)\}$;
6: Running Algorithm 1;
7: Increase k by 1;
8: Return the estimated parameters $\widehat{\boldsymbol{\theta}}^{\mathrm{T}}(k) = \widehat{\boldsymbol{\theta}}^{\mathrm{T}}$;
9: **end while**
10: **while** $T/\Delta T < k \leq N$ **do**
11: Specifies the initial number of iterations $p = 1$ and data length $N_T = T/\tau$;
12: Collecting the sampled data $\{\boldsymbol{x}(k - T/\Delta T), \ldots, \boldsymbol{x}(k - T/\Delta T + p)\}$ and $\{\boldsymbol{u}(k - T/\Delta T), \ldots, \boldsymbol{u}(k - T/\Delta T + p)\}$;
13: Running Algorithm 1;
14: Increase k by 1;
15: Return the estimated parameters $\widehat{\boldsymbol{\theta}}^{\mathrm{T}}(k) = \widehat{\boldsymbol{\theta}}^{\mathrm{T}}$;
16: **end while**
17: **return** $\widehat{\boldsymbol{\theta}}^{\mathrm{T}}(k)$;

IV. Convergence Analysis

This section presents a detailed convergence analysis of the DPI algorithm for modeling both autonomous and nonautonomous systems. Moreover, it takes into full account the impact of noise interference in practical working environments.

A. Autonomous System Without Noise Interference

The convergence analysis of the proposed algorithm in the autonomous system without noise interference is presented in the following theorem.

Theorem 2: Based on the different forms of parameter estimates (13), (16), and (20) obtained by the DPI algorithm in the autonomous system (10) for cases 1, 2, and 3. The parameter estimates of the proposed algorithm converges completely when the number of iterations satisfies $p \geq j$ in the environment without noise interference, and the parameter estimate is given by

$$
\widehat{\boldsymbol{\theta}}^{\mathrm{T}} = \boldsymbol{E_j}^{-1}\boldsymbol{X_j}. \qquad (28)
$$

Proof: Since the system parameter $\boldsymbol{\theta}$ does not varies with time, the following equation always holds, as:

$$
\boldsymbol{x}(t_p)^{\mathrm{T}} = \boldsymbol{e}\big(\boldsymbol{x}(t_{p-1}), \boldsymbol{u}(t_{p-1}), \boldsymbol{I}_{1\times 1}\big)^{\mathrm{T}}\boldsymbol{\theta}^{\mathrm{T}} \qquad (29)
$$

where p represents the number of iterations. If $p = j$, based on (11) and (12), we have

$$
\boldsymbol{X_j} = \boldsymbol{E_j}\boldsymbol{\theta}^{\mathrm{T}}. \qquad (30)
$$

From (16), the system parameters can be uniquely estimated, and these parameter estimates are equal to the true values because there is no noise interference in the system

$$
\widehat{\boldsymbol{\theta}}_{\boldsymbol{j}}^{\mathrm{T}} = \boldsymbol{\theta}^{\mathrm{T}} = \boldsymbol{E}_{\boldsymbol{j}}^{-1}\boldsymbol{X_j}. \qquad (31)
$$

Similarly, if $p > j$, based on (11) and (12), we obtain

$$
\underbrace{\begin{bmatrix} \boldsymbol{x}(t_p)^{\mathrm{T}} \\ \vdots \end{bmatrix}}_{\boldsymbol{X_j}} = \underbrace{\begin{bmatrix} \boldsymbol{e}\big(\boldsymbol{x}(t_{p-1}), \boldsymbol{u}(t_{p-1}), \boldsymbol{I}_{1\times 1}\big)^{\mathrm{T}} \\ \vdots \end{bmatrix}}_{\boldsymbol{E_j}}\boldsymbol{\theta}^{\mathrm{T}}. \qquad (32)
$$

Based on Definition 2 and Lemma 2, in this case, the estimated system parameter values need satisfy

$$
\left\|\boldsymbol{X_p} - \boldsymbol{E_p}\widehat{\boldsymbol{\theta}}_{\boldsymbol{p}}^{\mathrm{T}}\right\|_2^2 = \min\left\|\boldsymbol{X_p} - \boldsymbol{E_p}\boldsymbol{\theta}^{\mathrm{T}}\right\|_2^2. \qquad (33)
$$

In an environment without noise interference, the system state at each moment strictly adheres to (29), resulting in a least squares solution for the system parameters as $\widehat{\boldsymbol{\theta}}_{\boldsymbol{p}}^{\mathrm{T}} = \boldsymbol{\theta}^{\mathrm{T}}$.

Therefore, the parameter matrix estimation of the proposed algorithm for the autonomous system without noise interference can be expressed as

$$\widehat{\boldsymbol{\theta}}^{\mathrm{T}} = \boldsymbol{\theta}^{\mathrm{T}} = \boldsymbol{E_j}^{-1}\boldsymbol{X_j}. \tag{34}$$

This completes the proof of Theorem 2. ∎

B. Autonomous System With Noise Interference

In practical working conditions, quantum instrumentation typically employs bandpass filters to mitigate noise interference within specific frequency bands. Nevertheless, it is imperative to acknowledge that the influence of measurement noise remains inevitable. Therefore, it is necessary to analyze the convergence of the algorithm in this case.

Assumption 1: The measurement noise in quantum instrumentation consists of uncorrelated sequences of stochastic variables, each having an expected value and variance, and they all share a common upper and lower bound.

Assumption 2: Nonlinear transformations and combinations of measurement noise do not destroy the boundedness of the expectation and variance of each stochastic variable in them.

First, based on Assumptions 1 and 2 and (12), the autonomous system with noise interference can be expressed as follows:

$$\boldsymbol{X_p^*} = \boldsymbol{E_p^*}\boldsymbol{\theta}^{\mathrm{T}} \tag{35}$$

where $\boldsymbol{X_p^*} = \boldsymbol{X_p} + \boldsymbol{W_x^p}$ represents the observed system state iteration matrix, and $\boldsymbol{E_p^*} = \boldsymbol{E_p} + \boldsymbol{W_e^p}$ signifies the observed system nonlinear combination iteration matrix. The observed noise iteration matrix is defined as follows:

$$\boldsymbol{W_x^p} = \begin{bmatrix} \boldsymbol{w}_x(t_p)^{\mathrm{T}} \\ \vdots \\ \boldsymbol{w}_x(t_1)^{\mathrm{T}} \end{bmatrix} = \begin{bmatrix} w_x^1(t_p) & \cdots & w_x^n(t_p) \\ \vdots & \ddots & \vdots \\ w_x^1(t_1) & \cdots & w_x^n(t_1) \end{bmatrix}$$
$$\boldsymbol{W_e^p} = \begin{bmatrix} \boldsymbol{w}_e(t_p)^{\mathrm{T}} \\ \vdots \\ \boldsymbol{w}_e(t_1)^{\mathrm{T}} \end{bmatrix} = \begin{bmatrix} w_e^1(t_p) & \cdots & w_e^j(t_p) \\ \vdots & \ddots & \vdots \\ w_e^1(t_1) & \cdots & w_e^j(t_1) \end{bmatrix}. \tag{36}$$

Here, $\{w_x^r(t_1), w_x^r(t_2), \ldots, w_x^r(t_p)\}$ (for $1 \leq r \leq n$) and $\{w_e^t(t_1), w_e^t(t_2), \ldots, w_e^t(t_p)\}$ (for $1 \leq t \leq j$) represent sequences of uncorrelated stochastic variables, respectively. The expectations and variances of each stochastic variable $w_x^r(t_k)$ and $w_e^t(t_k)$ exist and share identical upper and lower bounds within their respective sequences.

Further, the following theorem presents a convergence analysis of autonomous systems with noise interference.

Theorem 3: Based on the DPI algorithm in cases 1, 2, and 3, we have derived different forms of parameter estimation (13), (16), and (20) for an autonomous system (35) with noisy interference. The parameter estimation of the proposed algorithm converges as the number of iterations $p \to \infty$.

Proof: Based on Definition 2 and Lemma 2, when $p > j$, the parameter estimate for (35) is as follows:

$$\widehat{\boldsymbol{\theta}} = \arg\min_{\boldsymbol{\theta}} \left\| \boldsymbol{X_p^*} - \boldsymbol{E_p^*}\boldsymbol{\theta}^{\mathrm{T}} \right\|_2^2. \tag{37}$$

Further, the least square solution can be obtained as

$$\widehat{\boldsymbol{\theta}}^{\mathrm{T}} = \left(\boldsymbol{E_p^*}^{\mathrm{T}}\boldsymbol{E_p^*}\right)^{-1}\boldsymbol{E_p^*}^{\mathrm{T}}\boldsymbol{X_p^*}. \tag{38}$$

We can decompose (38) into two parts, denoted as

$$\begin{aligned}\boldsymbol{E_p^*}^{\mathrm{T}}\boldsymbol{E_p^*} = \boldsymbol{E_p}^{\mathrm{T}}\boldsymbol{E_p} &+ \sum_{k=1}^{p}\boldsymbol{w}_e(t_k)\boldsymbol{w}_e(t_k)^{\mathrm{T}} \\ &+ \sum_{k=1}^{p}\boldsymbol{e}(\boldsymbol{x}(t_{k-1}), \boldsymbol{u}(t_{k-1}), \boldsymbol{I}_{1\times 1})\boldsymbol{w}_e(t_k)^{\mathrm{T}} \\ &+ \sum_{k=1}^{p}\boldsymbol{w}_e(t_k)\boldsymbol{e}(\boldsymbol{x}(t_{k-1}), \boldsymbol{u}(t_{k-1}), \boldsymbol{I}_{1\times 1})^{\mathrm{T}}\end{aligned} \tag{39}$$

and

$$\begin{aligned}\boldsymbol{E_p^*}^{\mathrm{T}}\boldsymbol{X_p^*} = \boldsymbol{E_p}^{\mathrm{T}}\boldsymbol{X_p} &+ \sum_{k=1}^{p}\boldsymbol{w}_e(t_k)\boldsymbol{w}_x(t_k)^{\mathrm{T}} \\ &+ \sum_{k=1}^{p}\boldsymbol{e}(\boldsymbol{x}(t_{k-1}), \boldsymbol{u}(t_{k-1}), \boldsymbol{I}_{1\times 1})\boldsymbol{w}_x(t_k)^{\mathrm{T}} \\ &+ \sum_{k=1}^{p}\boldsymbol{w}_e(t_k)\boldsymbol{x}(t_k)^{\mathrm{T}}.\end{aligned} \tag{40}$$

Applying Chebyshev's inequality and the law of large numbers [34] to (39) and (40), respectively, we obtain

$$\lim_{p\to\infty} P\left(\left|\frac{1}{p}\left(\boldsymbol{E_p^*}^{\mathrm{T}}\boldsymbol{E_p^*}\right)_{i,l} - \frac{1}{p}\boldsymbol{F}_{i,l}\right| > \boldsymbol{\alpha}_{i,l}\right) = 0 \tag{41}$$

and

$$\lim_{p\to\infty} P\left(\left|\frac{1}{p}\left(\boldsymbol{E_p^*}^{\mathrm{T}}\boldsymbol{X_p^*}\right)_{g,h} - \frac{1}{p}\boldsymbol{M}_{g,h}\right| > \boldsymbol{\beta}_{g,h}\right) = 0. \tag{42}$$

Here, $\boldsymbol{\alpha} \in \mathbb{R}^{j\times j}$ and $\boldsymbol{\beta} \in \mathbb{R}^{j\times n}$ are matrices whose elements are arbitrarily positive number. The other terms in (41) and (42) are defined as follows:

$$\begin{aligned}\boldsymbol{F} = \boldsymbol{E_p}^{\mathrm{T}}\boldsymbol{E_p} &+ \sum_{k=1}^{p}E\left(\boldsymbol{w}_e(t_k)\boldsymbol{w}_e(t_k)^{\mathrm{T}}\right) \\ &+ \sum_{k=1}^{p}\boldsymbol{e}(\boldsymbol{x}(t_{k-1}), \boldsymbol{u}(t_{k-1}), \boldsymbol{I}_{1\times 1})E\left(\boldsymbol{w}_e(t_k)^{\mathrm{T}}\right) \\ &+ \sum_{k=1}^{p}E(\boldsymbol{w}_e(t_k))\boldsymbol{e}(\boldsymbol{x}(t_{k-1}), \boldsymbol{u}(t_{k-1}), \boldsymbol{I}_{1\times 1})^{\mathrm{T}}\end{aligned} \tag{43}$$

and

$$\begin{aligned}\boldsymbol{M} = \boldsymbol{E_p}^{\mathrm{T}}\boldsymbol{X_p} &+ \sum_{k=1}^{p}E\left(\boldsymbol{w}_e(t_k)\boldsymbol{w}_x(t_k)^{\mathrm{T}}\right) \\ &+ \sum_{k=1}^{p}\boldsymbol{e}(\boldsymbol{x}(t_{k-1}), \boldsymbol{u}(t_{k-1}), \boldsymbol{I}_{1\times 1})E\left(\boldsymbol{w}_x(t_k)^{\mathrm{T}}\right) \\ &+ \sum_{k=1}^{p}E(\boldsymbol{w}_e(t_k))\boldsymbol{x}(t_k)^{\mathrm{T}}.\end{aligned} \tag{44}$$

Considering the correlation between the various nonlinear combinations chosen, we can express each element of the second term on the right-hand side of (43) and (44) as

$$E\left(w_e^i(t_k)w_e^l(t_k)\right) = E\left(w_e^i(t_k)\right) \cdot E\left(w_e^l(t_k)\right)$$

$$+\operatorname{Cov}\Big(w_e^i(t_k), w_e^l(t_k)\Big)$$
$$\leq E\big(w_e^i(t_k)\big)\cdot E\Big(w_e^l(t_k)\Big)$$
$$+\sqrt{\operatorname{Var}\big(w_e^i(t_k)\big)\cdot\operatorname{Var}\big(w_e^l(t_k)\big)} \quad (45)$$

and

$$E\Big(w_e^g(t_k)w_x^h(t_k)\Big) = E\big(w_e^g(t_k)\big)\cdot E\Big(w_x^h(t_k)\Big)$$
$$+\operatorname{Cov}\Big(w_e^g(t_k), w_x^h(t_k)\Big)$$
$$\leq E\big(w_e^g(t_k)\big)\cdot E\Big(w_x^h(t_k)\Big)$$
$$+\sqrt{\operatorname{Var}\big(w_e^g(t_k)\big)\cdot Var\big(w_x^h(t_k)\big)}. \quad (46)$$

Based on Assumptions 1 and 2 and (45) and (46), it becomes evident that matrices $\boldsymbol{F}$ and $\boldsymbol{M}$ exist and are bounded. Consequently, by utilizing (41) and (42), we can affirm that the parameter estimation matrix converges with a probability of 1 as the number of iterations $p \to \infty$, denoted as

$$\lim_{p\to\infty} P\left(\left|\widehat{\boldsymbol{\theta}^{\mathrm{T}}}_{i,h} - \left(\boldsymbol{F}^{-1}\boldsymbol{M}\right)_{i,h}\right| > \left(\boldsymbol{\alpha}^{-1}\boldsymbol{\beta}\right)_{i,h}\right) = 0. \quad (47)$$

This completes the proof of Theorem 3. ■

The above theorem indicates that in autonomous systems with noise interference, the proposed algorithm converges to the true value as the number of iterations p tends to infinity. However, performing an infinite number of iterations is impractical in real-world applications due to the resulting infinite extension of computational time.

To enhance computational efficiency in engineering applications, termination conditions are essential. These include halting the algorithm when the iteration count exceeds a threshold z or when the Frobenius norm between parameter matrices from consecutive iterations falls below a threshold ϱ. These procedures significantly reduce computational time while maintaining solution proximity to the true value.

C. Nonautonomous System Without Noise Interference

The convergence analysis of the DPI algorithm in the nonautonomous system provided without noise interference in the following corollary.

Corollary 2: Based on Algorithm 2 and Theorem 2, the convergence analysis of the proposed DPI algorithm for modeling nonlinear nonautonomous systems without noise interference can be categorized into the following four cases: 1) if $\tau > (T/j)$, the algorithm does not achieve convergence over all time steps; 2) if $\tau \leq (T/j)$ and $T \leq \Delta T$, then the algorithm achieves convergence over all time steps; 3) if $\tau \leq (\Delta T/j)$ and $\Delta T < T$, then the algorithm achieves convergence over all time steps; and 4) if $(\Delta T/j) < \tau \leq (T/j)$, then the algorithm achieves convergence within the time interval $[v\Delta T, N\Delta T]$, where $v = \lceil j(\tau/\Delta T)\rceil$.

Proof: If $\tau \geq (T/j)$, based on Theorem 1, fast sampling technique and Theorem 2, we can readily conclude that the proposed algorithm does not converge over all time steps.

If $\tau \leq (T/j)$, utilizing Algorithm 2 and Theorem 2, we observe that the estimation of the parameter matrix $\boldsymbol{\theta}(t_k)$ converges within any time interval $[t_{k+1} - T, t_{k+1}]$.

For case 2, when $\Delta T \geq T$, it is clear that $t_{k+1} - T \geq 0$ holds, and thus the time interval $[t_{k+1} - T, t_{k+1}]$ covers each estimation of the parameter matrix. We can conclude that the discrete model obtained using the proposed nonautonomous modeling approach converges completely.

For case 3, when $\tau \leq (\Delta T/j)$ and $\Delta T < T$, based on Algorithm 2 and Theorem 2, we can conclude that the estimation of the parameter matrices $\boldsymbol{\theta}(t_k)$ converges within the time interval $[t_{k+1} - \Delta T, t_{k+1}]$. Moreover, the condition $t_{k+1} - \Delta T \geq 0$ always holds, ensuring that the estimates of the parameter matrix converge over all time steps.

For case 4, when $(\Delta T/j) < \tau \leq (T/j)$, based on Algorithm 2 and Theorem 2, the estimation of the parameter matrix $\boldsymbol{\theta}(t_k)$ converges in the time interval $[t_{k+1} - j\tau, t_{k+1}]$. Since time is always non-negative, the condition $t_{k+1} - j\tau \geq 0$ is satisfied. Therefore, the time interval over which the parameter matrix estimates converge is $[v\Delta T, N\Delta T]$, where $v = \lceil j(\tau/\Delta T)\rceil$. ■

Based on the above citation, while theoretically minimizing τ for achieving convergence at all time steps is possible, practical applications necessitate the consideration of hardware performance limitations. These include the sampling rate constraints of the ADC, as well as the processing time limitations of the processor ($T_c \leq \Delta T$, where T_c represents the computational time of the processor for a single estimate of the parameter matrix).

D. Nonautonomous System With Noise Interference

According to Theorem 3 and the termination condition, it is assumed that in the worst case, the estimation of the parameter matrix needs to reach at least z ($z \geq j$) iterations before the proposed DPI algorithm can be considered converged. Combined with Corollary 2, we can derive the following corollary for analyzing the convergence of nonautonomous systems with noise interference.

Corollary 3: Based on Theorem 3 and Corollary 2, we consider the worst-termination condition and analyze the convergence of the proposed DPI algorithm for modeling nonlinear nonautonomous systems with noise interference, which can be divided into the following four cases: 1) if $\tau > (T/z)$, the algorithm does not achieve convergence over all time steps; 2) if $\tau \leq (T/z)$ and $T \leq \Delta T$, then the algorithm achieves convergence over all time steps; 3) if $\tau \leq (\Delta T/z)$ and $\Delta T < T$, then the algorithm achieves convergence over all time steps; and 4) if $(\Delta T/z) < \tau \leq (T/z)$, then the algorithm achieves convergence within the time interval $[s\Delta T, N\Delta T]$, where $s = \lceil z(\tau/\Delta T)\rceil$.

Proof: This nonautonomous system modeling process uses Algorithm 2. The distinction from Corollary 2 is the selection of a critical number of iterations z, which satisfies $z \geq j$.

The proof follows the pattern of Corollary 2 and is omitted for brevity. ■

Compared to Corollary 2, modeling nonautonomous systems with noise interference places higher demands on hardware performance to achieve algorithm convergence over all time steps. Hence, for practical applications, it is

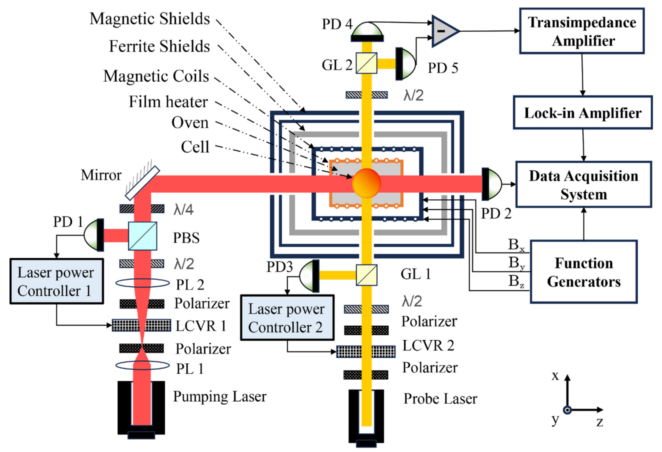

Fig. 2. Structure diagram of quantum instrumentation.

recommended to conduct an initial hardware assessment to determine an appropriate fast sampling time τ.

V. Simulation Validation

The proposed approach is validated for quantum instrumentation through numerical simulations of an optical pump magnetometer, implemented in MATLAB (R2020b), which relies on magnetic resonance for magnetic field measurements. Fig. 2 illustrates the structure diagram.

The dynamic evolution of the OPM system is depicted by (1) and (2), expandable as follows:

$$\frac{\mathrm{d}}{\mathrm{d}t}\boldsymbol{S} = \gamma \boldsymbol{B} \times \boldsymbol{S} - \boldsymbol{R}_{\text{tot}} \cdot (\boldsymbol{S} - \boldsymbol{S}_0). \tag{48}$$

Here, $\boldsymbol{S} = [S_x, S_y, S_z]^{\mathrm{T}}$ denotes the spin polarization of the atoms. $\boldsymbol{B} = [B_x, B_y, B_z]^{\mathrm{T}}$ represents the magnetic field felt by the atoms, where $B_z = B_0$ is the magnetic field to be measured in the z-direction, and $B_y = 2B_1 \cos(wt)$ signifies the AC excitation field applied in the y-direction with frequency w. Additionally, γ stands for the gyromagnetic ratio, $\boldsymbol{R}_{\text{tot}} = [R_2, R_2, R_1]^{\mathrm{T}}$ denotes the relaxation rate of the atoms, and $\boldsymbol{S}_0 = [0, 0, R_p/R_1]^{\mathrm{T}}$ signifies the steady-state polarization, where R_p is the pump rate of the pump beam.

A. Simulation Step

In practical operation, the limitations of the optics inevitably introduce pumping effects of the transverse probe beam on alkali metal atoms. In theoretical modeling (48), directly decoupling the measured longitudinal magnetic field from the nuclear magnetic resonance effect is intricate. To simplify calculations, a rotating coordinate system (x', y', z) with angular velocity ω is necessary. Here, is a simulation model of the dynamical evolution of atoms

$$\frac{\mathrm{d}}{\mathrm{d}t}\boldsymbol{S}' = \boldsymbol{U} \times \boldsymbol{S}' - \boldsymbol{R}_{tot} \cdot \left(\boldsymbol{S}' - \boldsymbol{S}_0'\right). \tag{49}$$

Here, $\boldsymbol{S}' = [S_{x'}, S_{y'}, S_z]^T$ is the polarization of alkali metal atoms in the x'-, y'-, and z-direction. $\boldsymbol{U} = [0, \phi, \Delta\omega]^T$ is the system input, where $\phi = \gamma B_1$ represents the amplitude of the AC excitation field, and $\Delta\omega = \gamma B_0 - \omega$ denotes the frequency difference between the Larmor precession of alkali metal atoms and the AC excitation field. $\boldsymbol{S}_0' = [R_{mx}/R_2, R_{my}/R_2, R_p/R_1]^T$ is the steady-state polarization.

TABLE I
Parameters of the OPM System

Parameter	Nominal Value	Parameter	Nominal Value
R_1	$1.89 \times 10^3\ \mathrm{s}^{-1}$	R_2	$1.57 \times 10^3\ \mathrm{s}^{-1}$
R_{mx}	$1.89\ \mathrm{s}^{-1}$	R_{my}	$0.63\ \mathrm{s}^{-1}$
R_p	$942.48\ s^{-1}$	B_1	0.1 nT

In this simulation, Rb atoms were selected as the alkali metal species, characterized by a gyromagnetic ratio of $\gamma = 2\pi \times 28\ \mathrm{Hz\,nT}^{-1}$. Remaining system parameters were determined from independent physical experiments, as detailed in Table I. To showcase the flexibility of input signal selection in our modeling approach, system input signals $\Delta\omega$ and ϕ were defined as random signals generated using the 'rand()' function in MATLAB.

B. Autonomous System Modeling

Alkali metal atoms exhibit rapid response rates, and to efficiently investigate their properties, we select discrete time intervals of $\Delta T = 5 \times 10^{-4}$ s and data lengths of $T = 0.1$ s. Based on the operating principles of the OPM, we can choose the following nonlinear combinatorial matrix:

$$\boldsymbol{e}(\boldsymbol{S}(t_k), \boldsymbol{u}(t_k), \boldsymbol{I}_{1\times 1}) = \begin{bmatrix} S_{x'}(t_k) \\ S_{y'}(t_k) \\ S_z(t_k) \\ \Delta w(t_k) S_{x'}(t_k) \\ \Delta w(t_k) S_{y'}(t_k) \\ \Delta w(t_k) S_z(t_k) \\ \phi(t_k) S_{x'}(t_k) \\ \phi(t_k) S_{y'}(t_k) \\ \phi(t_k) S_z(t_k) \\ 1 \end{bmatrix}. \tag{50}$$

The initial 70% of the total data obtained from the simulation is utilized for model training. Utilizing Algorithm 1, the resulting system parameter matrix is estimated as follows:

$$\widehat{\boldsymbol{\theta}}^T = \begin{bmatrix} 0.215 & 0.000 & 0.000 \\ 0.000 & 0.215 & 0.000 \\ 0.000 & 0.000 & 0.058 \\ 0.000 & -5.00 \times 10^{-4} & 0.000 \\ 5.00 \times 10^4 & 0.000 & 0.000 \\ 0.000 & 0.000 & 0.000 \\ 0.000 & 0.000 & 5.00 \times 10^{-4} \\ 0.000 & 0.000 & 0.000 \\ -5.00 \times 10^{-4} & 0.000 & 0.000 \\ 9.42 \times 10^{-4} & 3.14 \times 10^{-4} & 0.471 \end{bmatrix}. \tag{51}$$

The rotated coordinate system (x', y', z) is utilized for the theoretical model (48), while our developed DPI model predicts the remaining dataset. Simulation results in Fig. 3 validate the effectiveness of the proposed modeling approach in bridging the gap between theoretical and practical models.

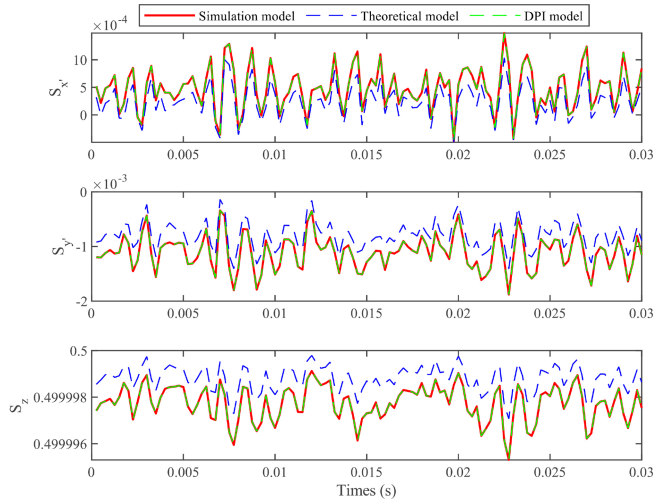

Fig. 3. Model output comparison for the autonomous system in the OPM system.

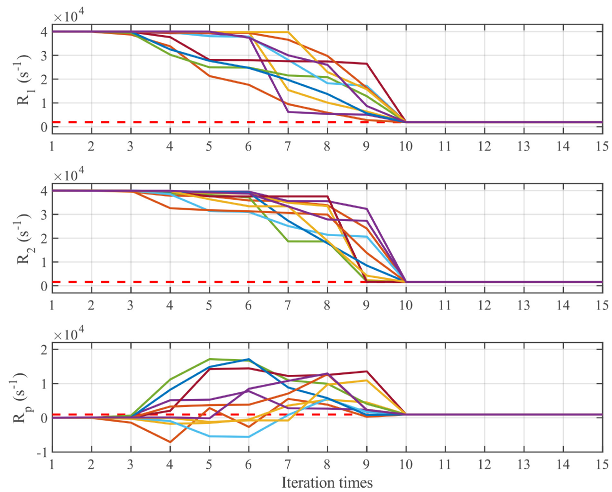

Fig. 4. Parameter estimation for the autonomous system: Solid lines indicate the estimated system parameters for different initial polarizations and dashed lines indicate the set values of the system parameters.

Based on the existing theoretical knowledge (48) and the chosen nonlinear combinatorial matrix (50), the system parameter matrix in the theoretical model can be derived as follows:

$$\boldsymbol{\theta}_t^T = \begin{bmatrix} 1-R_2\Delta T & 0 & 0 \\ 0 & 1-R_2\Delta T & 0 \\ 0 & 0 & 1-R_1\Delta T \\ 0 & -\Delta T & 0 \\ \Delta T & 0 & 0 \\ 0 & 0 & 0 \\ 0 & 0 & \Delta T \\ 0 & 0 & 0 \\ -\Delta T & 0 & 0 \\ 0 & 0 & R_p\Delta T \end{bmatrix}. \tag{52}$$

Combining (51) and (52) allows concurrent estimation of specific physical parameters in the practical system during modeling. To validate these estimates, ten experiments were conducted using an Intel Core i9-10900K processor with varying initial conditions, yielding an average computation time of 0.00067 s. Fig. 4 illustrates the convergence of parameter estimation to the set values after the 10th iteration. A comparison between (51) and (52) reveals two missing elements in the calculated theoretical parameter matrix. By incorporating the designed nonlinear combinatorial matrix (50), we rectify the theoretical model (48) as follows:

$$\frac{\mathrm{d}}{\mathrm{d}t}\boldsymbol{S} = \gamma \boldsymbol{B} \times \boldsymbol{S} - \boldsymbol{R}_{\mathrm{tot}} \cdot \left(\boldsymbol{S} - \boldsymbol{S}_0^*\right) \tag{53}$$

where $\boldsymbol{S}_0^* = [V_1, V_2, R_p/R_1]$. The physical interpretations of parameters V_1 and V_2 require further elucidation through experimental validation coupled with theoretical insights.

C. Nonautonomous System Modeling

Consider the following parameter change process:

$$R_p(t_k) = \begin{cases} 942.48\ \mathrm{s}^{-1} & 0\ \mathrm{ms} < t_k \le 30\ \mathrm{ms} \\ 1319.5\ \mathrm{s}^{-1} & 30\ \mathrm{ms} < t_k \le 70\ \mathrm{ms} \\ 1696.5\ \mathrm{s}^{-1} & 70\ \mathrm{ms} < t_k \le 100\ \mathrm{ms}. \end{cases} \tag{54}$$

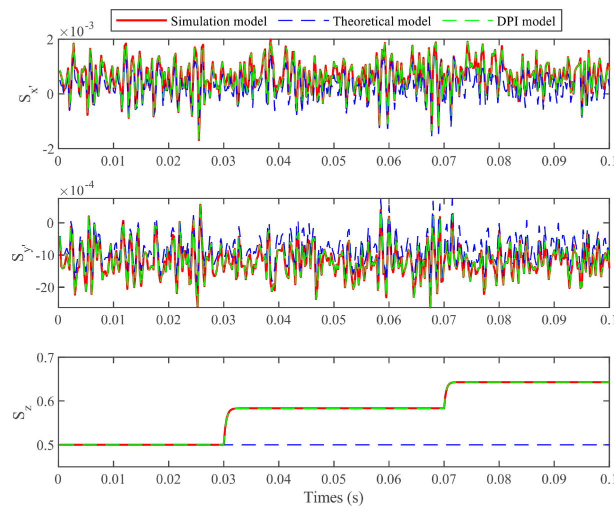

Fig. 5. ModelModel output comparison for the nonautonomous system in the OPM system.

This process extends the autonomous system by incorporating three distinct sets of system parameters, all of which remain the same as those of the autonomous system except for the varying pump rates.

Upon completing the modeling of the autonomous system using the DPI algorithm, we secure convergence at all time steps by employing a stabilization time of $T = 1 \times 10^{-4}$, s and a high-fast sampling rate of $F_s^{\mathrm{hig}} = 1 \times 10^5$, Hz in accordance with Corollary 2. Following this, Algorithm 2 is utilized for modeling the nonautonomous system.

Fig. 5 presents results for the system output from the simulation model, theoretical model, and our developed DPI model. Our approach adeptly addresses the challenge of modeling nonautonomous systems, particularly acquiring real-time physical parameters without disturbing the operational state of quantum instruments in practical applications.

The system is modeled under varying conditions of stabilization time and fast sampling rate to validate the effectiveness

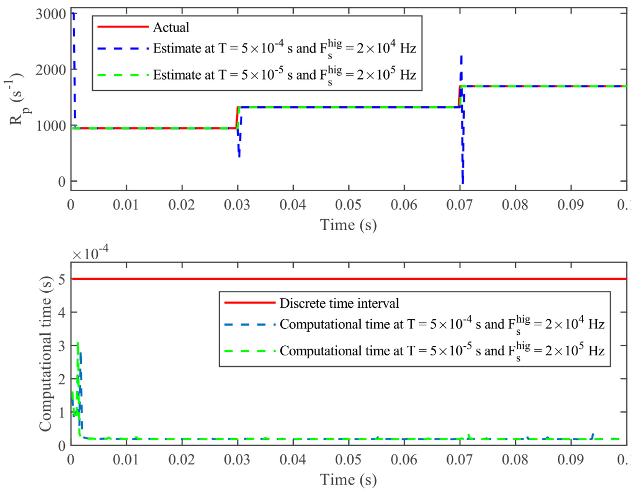

Fig. 6. Parameter estimation and corresponding computational time for nonautonomous systems in the OPM system.

of the algorithm. Corresponding system parameters are displayed in Fig. 6.

During this simulation, changes in the pump rate occur within discrete time intervals. An excessively extended stabilization time renders the proposed algorithm incapable of accurately modeling the system state during rapid fluctuations in system parameters. To address this challenge in practical applications, choose shorter stabilization times and larger fast sampling rates whenever possible.

Furthermore, Fig. 6 presents the calculation time for each iteration of Algorithm 2. During the initial phase of algorithm operation, factors, such as Just-In-Time compiler optimizations, memory management, and cache effects, contribute to a longer calculation time. As the algorithm operates, the calculation time significantly reduces. Since the matrix dimensions solved in each subsequent iteration remain constant, the calculation time remains nearly unchanged. It is important to note that this specific variation in calculation time is independent of the time complexity of the algorithm itself. Thus, in practical applications, we can mitigate this unfavorable phenomenon by preheating the hardware and software in advance.

VI. Experimental Validation

In this section, we utilize the DPI modeling approach for the SERFCM. Fig. 2 illustrates the structural diagram. The dynamic behavior of the system is described based on (1) and (2)

$$\frac{\mathrm{d}\boldsymbol{P^e}}{\mathrm{d}t} = \boldsymbol{U^e} \times \boldsymbol{P^e} - \frac{R^e_{\mathrm{tot}}}{Q}\left(\boldsymbol{P^e} - \boldsymbol{P^e_0}\right) + \frac{R^{en}_{se}}{Q}\left(\boldsymbol{P^n} - \boldsymbol{P^e}\right)$$
$$\frac{\mathrm{d}\boldsymbol{P^n}}{\mathrm{d}t} = \boldsymbol{U^n} \times \boldsymbol{P^n} - R^n_{\mathrm{tot}}\left(\boldsymbol{P^n} - \boldsymbol{P^n_0}\right) + R^{ne}_{se}\left(\boldsymbol{P^e} - \boldsymbol{P^n}\right). \quad (55)$$

Here, $\boldsymbol{P^e} = [P^e_x, P^e_y, P^e_z]^T$ and $\boldsymbol{P^n} = [P^n_x, P^n_y, P^n_z]^T$ denote the spin polarizations of the alkali metal atoms and the noble gas atoms, respectively. R^e_{tot} and R^n_{tot} represent the relaxation rates of the alkali metal atoms and the noble gas atoms, respectively. R^{en}_{se} is the spin exchange rate per alkali metal atom, and R^{ne}_{se} is the spin exchange rate per noble gas atom.

TABLE II
Parameters of the SERFCM System

Parameter	Nominal Value	Parameter	Nominal Value
γ^e	$2\pi \times 28$ Hz nT^{-1}	γ^n	$2\pi\times3.36\times10^{-3}$ Hz nT^{-1}
R^e_{tot}	2262 s^{-1}	R^n_{tot}	2×10^{-4} s^{-1}
R_p	1068 s^{-1}	Q	6
λM^e	-60 nT	λM^n	-1.3×10^4 nT
R^{ne}_{se}	4×10^{-6} s^{-1}	B_c	-161.4 nT

$\boldsymbol{P^e_0} = [0, 0, R_p/R^e_{\mathrm{tot}}]^T$ and $\boldsymbol{P^n_0} = [0, 0, 0]^T$ represent the steady-state polarization of the alkali metal atoms and the noble gas atoms, respectively. Q is the nuclear slowing-down factor. The remaining terms in (55) are given by

$$\boldsymbol{U^e} = \frac{\gamma^e}{Q}\left(\boldsymbol{B} - \lambda M^n \boldsymbol{P^n}\right) + \boldsymbol{\Omega}$$
$$\boldsymbol{U^n} = \gamma^n\left(\boldsymbol{B} - \lambda M^e \boldsymbol{P^e}\right) + \boldsymbol{\Omega}. \quad (56)$$

Here, $\mathbf{B} = [B_x, B_y, B_c + B_z]^T$ represents the magnetic field in the cell. γ^e and γ^n represent the gyromagnetic ratios of the alkali metal atoms and the noble gas atoms, respectively. The magnetization of the alkali metal atoms is denoted as λM^e, and the magnetization of the noble gas atoms is denoted as λM^n, both indicating complete spin polarization. Furthermore, the vector $\Omega = [\Omega_x, \Omega_y, \Omega_z]^T$ represents the angular velocity.

A. Experimental Step

In this experiment, the K-Rb-^{21}Ne atomic ensemble is used with a discrete time interval of 0.005 s. In conjunction with the operating principle of the system, the transverse magnetic field B_x is employed as the excitation source. Initially, a constant input of 3.31 nT is set, and subsequently, after the system reaches a steady state, a random input with an amplitude of 1.5 nT and a frequency of 2 Hz is introduced. The parameters of the atomic ensemble are determined based on the results of independent experiments, as presented in Table II.

B. Autonomous System Modeling

In accordance with the described experimental conditions, we obtained system inputs and outputs for a duration of 30 s. Following the operational principle of SERFCM, we selected the subsequent nonlinear combinatorial matrix:

$$\boldsymbol{e}(\boldsymbol{S}(t_k), \boldsymbol{u}(t_k), \boldsymbol{I}_{1\times1}) = \begin{bmatrix} S^e_x(t_k) \\ S^e_y(t_k) \\ S^e_z(t_k) \\ B_x(t_k)S^e_x(t_k) \\ B_x(t_k)S^e_y(t_k) \\ B_x(t_k)S^e_z(t_k) \\ 1 \end{bmatrix}. \quad (57)$$

Using Algorithm 1, we formulated a DPI model for the system. To verify our proposed modeling approach, we compared it with the approach presented in [28] under identical conditions. Notably, 70% of the initial experimental data were used for model training in this experiment, while the remaining data was allocated for model prediction. Fig. 7 illustrates the system output prediction results of different models, and Table III provides corresponding comparative

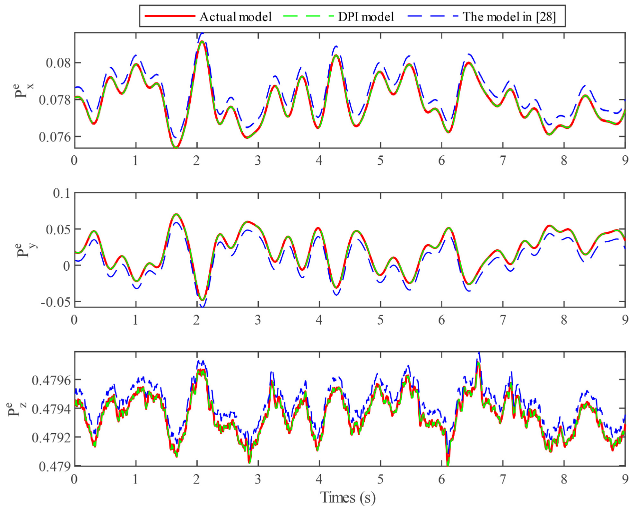

Fig. 7. Model output comparison for the autonomous system in the SERFCM.

TABLE III
ERROR SUMMARY FOR THE AUTONOMOUS SYSTEM EXPERIMENT

	P_x^e		P_y^e		P_z^e	
	MAPE	RMSE	MAPE	RMSE	MAPE	RMSE
DPI	0.061%	5.82×10^{-5}	3.1%	1.13×10^{-4}	0.031%	2.09×10^{-5}
[28]	0.67%	5.21×10^{-4}	27.1%	1.08×10^{-3}	0.17%	7.97×10^{-4}

analyses. The experimental results reveal that the developed DPI model demonstrates a smaller mean absolute percentage error (MAPE) and root mean square error (RMSE), primarily due to its applicability to nonlinear systems.

The proposed approach accurately models the system and estimates specific physical parameters, utilizing prior physical knowledge (55). Building upon the selected nonlinear combinatorial matrix (57), we derive the system parameter matrix within the theoretical model, expressed in (58), shown at the bottom of the page.

Considering practical noise interference, it often exhibits characteristics of Gaussian white noise [35] over short periods, with a standard deviation of approximately 1.46×10^{-4}. To study how the number of iterations affects system parameter estimation convergence, the model was trained with varying iterations, and system input and output were sampled at 2000 Hz. Combining the acquired system parameter matrix with (58) yields estimated model parameter values, along with corresponding computational times in Table IV.

The experimental results indicate that, with an increasing number of iterations, the estimated system parameters gradually approach the physical parameter values obtained from independent experiments. Simultaneously, the computational

TABLE IV
RESULTS OF THE MODEL PARAMETERS ESTIMATION

Iteration	Estimated model paramaters					Compute time
p	$\widehat{R_{tot}^e}(s^{-1})$	$\widehat{R_p}(s^{-1})$	$\widehat{P_x^n}$	$\widehat{P_y^n}$	$\widehat{P_z^n}$	$T_c(\mu s)$
500	1840	1262	3.73×10^{-5}	7.29×10^{-4}	0.012	62.63
1000	2214	1084	4.12×10^{-6}	1.81×10^{-5}	0.012	89.72
3000	2230	1076	4.00×10^{-6}	4.14×10^{-6}	0.012	123.84
9000	2237	1074	1.88×10^{-6}	3.28×10^{-6}	0.012	322.52
15000	2246	1070	8.81×10^{-7}	5.69×10^{-7}	0.011	528.69
[29]	2262	−−	−−	−−	−−	−−
[30]	−−	1068	−−	−−	−−	−−
[31]	−−	−−	−−	−−	0.010	−−

time also gradually increases. It is crucial to note that, in this context, we consider the system parameter values obtained from independent physical experiments as reference values, as obtaining the true parameter values of the practical system directly from the measurement perspective is not feasible. Finally, in comparison to existing physical parameter measurement approaches [29], [30], and [31], our approach has significant advantages in testing multiple physical parameters while maintaining the operating state of the system. This advantage stems from our parameter estimation approach, which imposes no limitations on the excitation signal.

C. Nonautonomous System Modeling

In this experiment, we adjust the pump laser power to achieve distinct system operating points. This identifies the SERFCM as a complex, nonlinear, nonautonomous system. Additionally, we record the inputs and outputs for 30 s.

Taking into consideration the convergence patterns of the proposed DPI model at different iteration numbers and the corresponding computation time, as illustrated in Table IV, we have limited the iterations of Algorithm 2 to a maximum of 1000. This choice aims to strike a balance between modeling accuracy and computational efficiency. To comprehensively capture the nonautonomous characteristics of the system, we have chosen a short stabilization time of $T = 0.05$ s and accordingly selected a fast sampling frequency of $F_s^{\text{high}} = 2 \times 10^4$ Hz. Leveraging Algorithm 2, we have successfully conducted online system modeling and carried out a comparative verification with the approach outlined in [28] under identical conditions. The system output prediction results for different models are presented in Fig. 8.

The experimental results demonstrate that the DPI model more precisely predicts the x-direction output during the initial stage of online modeling, capturing the nonlinear properties of the system effectively under the excitation source B_x. Furthermore, the DPI model accurately forecasts the output of the nonautonomous system under state changes, a capability

$$\boldsymbol{\theta}_t(t_k) = \begin{bmatrix} 1 - \frac{R_{\text{tot}}^e(t_k)}{Q}\Delta T & -\frac{\gamma_e}{Q}\left(\lambda M^n P_z^n(t_k) + B_c\right)\Delta T & \frac{\gamma_e}{Q}\lambda M^n P_y^n(t_k)\Delta T & 0 & 0 & 0 & 0 \\ \frac{\gamma_e}{Q}\left(\lambda M^n P_z^n(t_k) + B_c\right)\Delta T & 1 - \frac{R_{\text{tot}}^e(t_k)}{Q}\Delta T & -\frac{\gamma_e}{Q}\lambda M^n P_x^n(t_k)\Delta T & 0 & -\frac{\gamma_e}{Q}\Delta T & 0 & 0 \\ -\frac{\gamma_e}{Q}\lambda M^n P_y^n(t_k)\Delta T & \frac{\gamma_e}{Q}\lambda M^n P_x^n(t_k)\Delta T & 1 - \frac{R_{\text{tot}}^e(t_k)}{Q}\Delta T & 0 & 0 & \frac{\gamma_e}{Q}\Delta T & \frac{R_p(t_k)}{Q}\Delta T \end{bmatrix}. \tag{58}$$

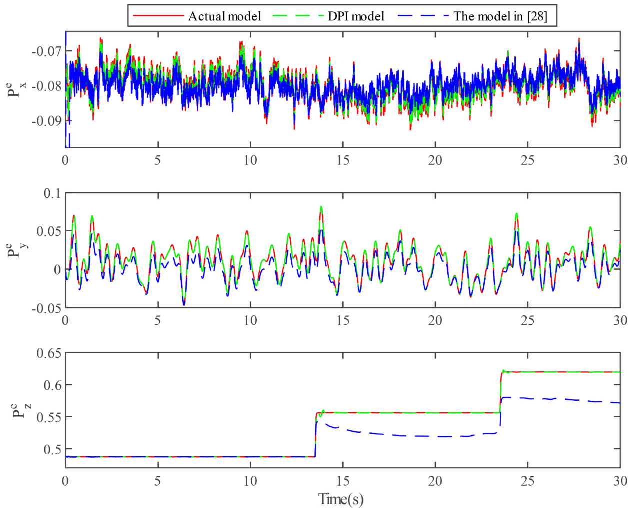

Fig. 8. Model output comparison for the nonautonomous system in the SERFCM.

TABLE V
ERROR SUMMARY OF THE NONAUTONOMOUS SYSTEM EXPERIMENT

	P_x^e		P_y^e		P_z^e	
	MAPE	RMSE	MAPE	RMSE	MAPE	RMSE
DPI	0.74%	7.86×10^{-3}	1.62%	2.81×10^{-3}	0.16%	6.19×10^{-3}
[28]	8.56%	0.101	48.7%	0.012	7.42%	0.029

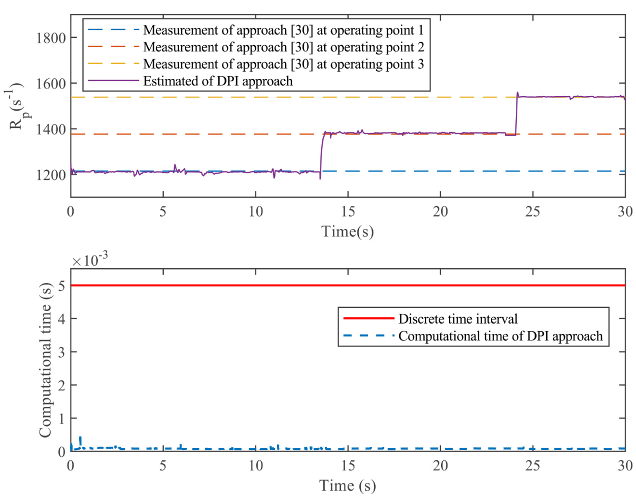

Fig. 9. Parameter estimation and corresponding computational time for nonautonomous systems in the SERFCM.

lacking in the approach presented in [28]. Comparative analysis results in Table V indicate a reduction in prediction errors with the DPI model proposed in this article.

The proposed approach also facilitates online estimation of dynamic system parameters. Fig. 9 depicts the estimated pump rates, comparing them with results from the approach in [30], obtained through offline measurements at varying pump laser power. The results highlight the superior online parameter estimation capabilities of the proposed approach without destroying the operating state of the system. Moreover, Fig. 9 presents the computational time for each modeling step, consistently below the predefined discrete time. This emphasizes the efficiency of the online modeling technique.

VII. CONCLUSION

This article proposes an effective online modeling approach for quantum instrumentation with nonlinear and nonautonomous characteristics. The developed approach contributes significantly in two main aspects: 1) from a cybernetic perspective, it addresses the interpretability issues associated with traditional data-driven modeling approaches and 2) from an experimental physics viewpoint, it represents the first attempt to tackle the data-driven modeling problem in quantum instrumentation. This breakthrough overcomes the limitations of traditional physics experiments where simultaneous estimation of multiple physical parameters is challenging. The effectiveness of the proposed approach is validated through simulations and experiments.

The DPI modeling approach surpasses traditional data-driven approaches in terms of reasonability and advancement. However, it requires a certain level of physics knowledge and engineering experience and is not applicable to nonstationary stochastic systems. Future extensions of this study aim to encompass other complex physical systems, such as superconducting quantum interference device magnetometers and nitrogen-vacancy center ensembles.

REFERENCES

[1] B. Dmitry and R. Michael, "Optical magnetometry," *Nat. Phys.*, vol. 3, no. 4, pp. 227–234, 2007.
[2] R. Lange et al., "Improved limits for violations of local position invariance from atomic clock comparisons," *Phys. Rev. Lett.*, vol. 126, Jan. 2021, Art. no. 011102.
[3] R. Zhang et al., "Recording brain activities in unshielded earth's field with optically pumped atomic magnetometers," *Sci. Adv.*, vol. 6, no. 24, 2020, Art. no. eaba8792.
[4] I. K. Kominis, T. W. Kornack, J. C. Allred, and M. V. Romalis, "A subfemtotesla multichannel atomic magnetometer," *Nature*, vol. 422, no. 6932, pp. 596–599, 2003.
[5] Z. Wang et al., "Atomic spin polarization controllability analysis: A novel controllability determination method for spin-exchange relaxation-free co-magnetometers," *IEEE/CAA J. Autom. Sinica*, vol. 9, no. 4, pp. 699–708, Apr. 2022.
[6] G. Vasilakis, J. M. Brown, T. W. Kornack, and M. V. Romalis, "Limits on new long range nuclear spin-dependent forces set with a K-^{3}he comagnetometer," *Phys. Rev. Lett.*, vol. 103, no. 26, 2009, Art. no. 261801.
[7] M. Limes et al., "Portable magnetometry for detection of biomagnetism in ambient environments," *Phys. Rev. Appl.*, vol. 14, Jul. 2020, Art. no. 011002.
[8] E. Boto et al., "Measuring functional connectivity with wearable MEG," *NeuroImage*, vol. 230, Apr. 2021, Art. no. 117815.
[9] T. W. Kornack, R. K. Ghosh, and M. V. Romalis, "Nuclear spin gyroscope based on an atomic comagnetometer," *Phys. Rev. Lett.*, vol. 95, Nov. 2005, Art. no. 230801.
[10] D. Kim, M. I. Ibrahim, C. Foy, M. E. Trusheim, R. Han, and D. R. Englund, "A CMOS-integrated quantum sensor based on nitrogen-vacancy centres," *Nat. Electron*, vol. 2, pp. 284–289, Jul. 2019.
[11] J. Vaara and M. V. Romalis, "Calculation of scalar nuclear spin-spin coupling in a noble-gas mixture," *Phys. Rev. A*, vol. 99, Jun. 2019, Art. no. 060501.
[12] Z. Wang, R. Wang, S. Liu, L. Xing, and B. Qin, "Fractional exponential feedback control for finite-time stabilization and its application in a spin-exchange relaxation-free comagnetometer," *IEEE Trans. Cybern.*, vol. 53, no. 11, pp. 7008–7020, Nov. 2023.
[13] Y. Zhao, H. Wang, N. Xu, G. Zong, and X. Zhao, "Reinforcement learning-based decentralized fault tolerant control for constrained interconnected nonlinear systems," *Chaos Solitons Fract*, vol. 167, Feb. 2023, Art. no. 113034.
[14] T. W. Kornack and M. V. Romalis, "Dynamics of two overlapping spin ensembles interacting by spin exchange," *Phys. Rev. Lett.*, vol. 89, Dec. 2002, Art. no. 253002.

[15] B. A. Brown, G. F. Bertsch, L. M. Robledo, M. V. Romalis, and V. Zelevinsky, “Nuclear matrix elements for tests of local lorentz invariance violation,” *Phys. Rev. Lett.*, vol. 119, Nov. 2017, Art. no. 192504.
[16] K. Wei et al., “Simultaneous determination of the spin polarizations of noble-gas and alkali-metal atoms based on the dynamics of the spin ensembles,” *Phys. Rev. Appl.*, vol. 13, Apr. 2020, Art. no. 044027.
[17] J. Geiger, A. Sabadell-Rendón, N. Daelman, and L. Núria, “Data-driven models for ground and excited states for single atoms on ceria,” *Npj Comput. Mater.*, vol. 8, p. 171, Aug. 2022.
[18] S. Liu, B. Niu, G. Zong, X. Zhao, and N. Xu, “Data-driven-based event-triggered optimal control of unknown nonlinear systems with input constraints,” *Nonl. Dyn.*, vol. 109, no. 2, pp. 891–909, 2022.
[19] L. Gao, D. Li, L. Yao, and Y. Gao, “Sensor drift fault diagnosis for chiller system using deep recurrent canonical correlation analysis and *k*-nearest neighbor classifier,” *ISA Trans.*, vol. 122, pp. 232–246, Mar. 2022.
[20] H. Luo and S. G. Paal, “A data-free, support vector machine-based physics-driven estimator for dynamic response computation,” *Comput.-Aided Civ. Infrastruct. Eng.*, vol. 38, no. 1, pp. 26–48, 2022.
[21] J. Ma, B. Huang, and F. Ding, “Iterative identification of Hammerstein parameter varying systems with parameter uncertainties based on the variational Bayesian approach,” *IEEE Trans. Syst., Man., Cybern., Syst.*, vol. 50, no. 3, pp. 1035–1045, Mar. 2020.
[22] Y. Zhang, A. Li, B. Deng, and K. K. Hughes, “Data-driven predictive models for chemical durability of oxide glass under different chemical conditions,” *Npj Comput. Mater.*, vol. 4, no. 14, pp. 2397–2106, 2020.
[23] T. Matthias and Z. Z. Jun, “Wind turbine modeling with data-driven methods and radially uniform designs,” *IEEE Trans. Ind. Informat.*, vol. 12, no. 3, pp. 1261–1269, Jun. 2016.
[24] X. Lai et al., “Capacity estimation of lithium-ion cells by combining model-based and data-driven methods based on a sequential extended Kalman filter,” *Energy*, vol. 216, Feb. 2021, Art. no. 119233.
[25] E. Vanem, C. B. Salucci, A. Bakdi, and Ø. Å. Alnes, “Data-driven state of health modelling-A review of state of the art and reflections on applications for maritime battery systems,” *J. Energy Storage*, vol. 43, Nov. 2021, Art. no. 103158.
[26] J. Li, C. Hua, Y. Yang, and X. Guan, “Data-driven Bayesian-based Takagi–Sugeno fuzzy modeling for dynamic prediction of hot metal silicon content in blast furnace,” *IEEE Trans. Syst., Man., Cybern., Syst.*, vol. 52, no. 2, pp. 1087–1099, Feb. 2022.
[27] M. S. Safronova, D. Budker, D. DeMille, D. F. J. Kimball, A. Derevianko, and C. W. Clark, “Search for new physics with atoms and molecules,” *Rev. Mod. Phys.*, vol. 90, Jun. 2018, Art. no. 025008.
[28] Q. Wu, S. Dong, W.-A. Zhang, and L. Yu, “Online modeling of the CNC engraving system with dead-zone input nonlinearity,” *IEEE Trans. Ind. Electron.*, vol. 69, no. 1, pp. 774–782, Jan. 2022.
[29] M. E. Limes, D. Sheng, and M. V. Romalis, “^{3}he-^{129}Xe comagnetometery using ^{87}Rb detection and decoupling,” *Phys. Rev. Lett.*, vol. 120, Jan. 2018, Art. no. 033401.
[30] J. Liu et al., “Dynamics of a spin-exchange relaxation-free comagnetometer for rotation sensing,” *Phys. Rev. Appl.*, vol. 17, Jan. 2022, Art. no. 014030.
[31] K. Wei et al., “New constraints on exotic spin-velocity-dependent interactions,” *Nat. Commun.*, vol. 13, p. 7387, Nov. 2022.
[32] A. Ben-Israel and T. N. E. Greville, *Generalized Inverses: Theory and Applications*. New York, NY, USA: Springer, 2003.
[33] G. Wang, Y. Wei, S. Qiao, P. Lin, and Y. Chen, *Generalized Inverses: Theory and Computations*. Beijing, China: Springer, 2018.
[34] F. M. Dekking, C. Kraaikamp, H. P. Lopuhaä, and L. E. Meester, *A Modern Introduction to Probability and Statistics: Understanding Why and How*. London, U.K.: Springer, 2005.
[35] B. Qin, Z. Wang, R. Wang, F. Li, Z. Liu, and C. Fang, “Modeling of nonlinear and nonstationary stochasticity for atomic ensembles,” *ISA Trans.*, vol. 143, pp. 557–571, Dec. 2023.

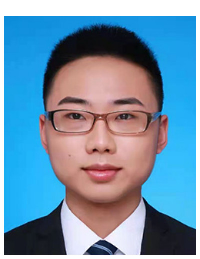

Bodong Qin received the B.E. degree in Mechanical Engineering from the School of Mechanical Electronic and Information Engineering, China University of Mining and Technology, Beijing, China, in 2019. He is currently pursuing the Ph.D. degree with the School of Instrumentation and Optoelectronic Engineering, Beihang University, Beijing.

His research interest includes modeling and control technology of comagnetometers operated in the spin-exchange relaxation-free regime.

Zhuo Wang received the B.E. degree in automation from Beihang University, Beijing, China, in 2006, and the Ph.D. degree in electrical and computer engineering from the University of Illinois at Chicago, Chicago, IL, USA, in 2013.

He was a Postdoctoral Fellow with the Department of Electrical and Computer Engineering, University of Alberta, Edmonton, AB, USA, from 2013 to 2014. He was a Research Assistant Professor with the Fok Ying Tung Graduate School, Hong Kong University of Science and Technology, Hong Kong, from 2014 to 2015. He was with Beihang University since 2016, and is currently a Professor and a Ph.D. Instructor with the School of Instrumentation and Optoelectronic Engineering, with the Key Laboratory of Ministry of Industry and Information Technology on Quantum Sensing Technology, with Beijing Advanced Innovation Center for Big Data-Based Precision Medicine, Beihang University, and also with Beihang Hangzhou Innovation Institute, Hangzhou, China. His research interests include data-based system identification, modeling, analysis, learning, and control; nonlinear system adaptive control; atomic spin ensembles system control; as well as state estimation and signal processing of complex high-precision measurement instruments.

Wenfeng Fan received the Ph.D. degree in precision instruments and mechanics from Beihang University, Beijing, China, in 2020.

He is currently engaged in postdoctoral research with the School of Instrumentation and Optoelectronic Engineering, Beihang University. His research interest is focused on the magnetic response of atomic magnetometer and comagnetometer operated in the spin-exchange relaxation-free regime.

Ruigang Wang received the B.E. degree in Measurement and Control Technology and Instrument from the School of Instrumentation and Optoelectronic Engineering, Hefei University of Technology, Hefei, China, in 2018, and the Ph.D. degree with the School of Instrumentation and Optoelectronic Engineering, Beihang University, Beijing, China, in 2023.

He is currently a Lecturer with the School of Information Science and Technology, Hangzhou Normal University, Hangzhou, China. His research interests include nonlinear control, and their applications in atomic ensembles.

Feng Li received the B.E. degree in Measurement and Control Technology and Instrument from the Shandong University of Science and Technology, Qingdao, China, in 2020. He is currently pursuing the Ph.D. degree with the School of Instrumentation and Optoelectronic Engineering, Beihang University, Beijing, China.

His research covers reinforcement learning, nonlinear control, and their application in the spin-exchange relaxation-free comagnetometers.

Wei Quan received the Ph.D. degree in precision instruments and mechanics from Beihang University, Beijing, China, in 2008.

He is currently a Professor with the Innovative Research Institute of Frontier Science and Technology and the Advanced Innovation Center for Biomedical Engineering, Beihang University. His research interests cover celestial navigation and the recently developed atomic inertial sensors based on alkali-metal vapor cell.